Physicochem. Probl. Miner. Process., 61(6), 2025, 215005

http://www.journalssystem.com/ppmp

Physicochemical Problems of Mineral Processing

ISSN 1643-1049

Research on the motion characteristics of flotation bubbles based on virtual binocular stereo vision technology

Liqiang Zhang [1,2], Dong Liu [1,2], Jinlong Liu[1, 2], Aijun Qian [1,2]

[1] Tangshan Research Institute of China Coal Technology & Engineering Group

, Tangshan, Hebei/Province, China, 063012;

[2] Hebei Province Coal Preparation Engineering & Technology Research Center, Tangshan, Hebei/Province, China, 063012.

Corresponding author: 605262112@qq.com (Aijun Qian)

Abstract: Understanding bubble kinematics in flotation is essential for process optimization, yet conventional two-dimensional (2D) imaging provides only limited descriptors. Here, bubbles in a column flotation system were examined using a custom-built virtual binocular stereovision platform that acquires dual-view images for stereoscopic characterization. The raw images were processed in MATLAB, and bubble parameters were extracted through camera calibration and coordinate transformation. The effects of reagent concentration and gas distributor orifice diameter on bubble velocity were quantified, and the relationships among velocity, equivalent diameter, and aspect ratio were analyzed. Results show that bubble velocity decreases with increasing reagent concentration and increases with larger orifice diameter. The concentration-induced reduction in velocity is markedly enhanced as the concentration increases from 1 to 2 mg/dm^3, and this effect is most pronounced for the 0.2-mm orifice. Peaks in instantaneous velocity coincide with minima in aspect ratio, indicating transient bubble elongation at high speed. Bubble velocity is positively correlated with equivalent diameter, and this scaling is independent of aperture size. These findings provide a mechanistic basis for tuning operating conditions in hematite column flotation. The findings provide a quantitative foundation for understanding bubble kinematics in flotation systems and contribute to improving mineral separation efficiency through more precise hydrodynamic regulation.

Keywords: flotation, virtual stereo vision, bubble movement, column flotation, three-dimensional measurement

1. Introduction

In flotation, bubbles serve as the transport carriers of mineral particles at the gas–liquid interface; their formation, size, shape, and dynamic behavior directly determine the bubble surface area flux (S_b), thereby governing the probabilities of effective particle–bubble collision and attachment (Han et al., 2023a). The molecular structure and concentration of the frother, the chemical environment of the pulp, and the aeration mode of the flotation unit can markedly alter the Sauter mean bubble diameter (d_{32}) and the gas holdup, thus affecting the flotation rate constant and separation selectivity. Therefore, quantitative investigation of the multiscale coupling among reagents, equipment, and bubble swarms is essential for improving flotation performance and achieving process scale-up.

Recent studies have focused on regulating bubble populations through controllable operating variables. Panjipour et al. (2021) systematically varied frother dosage, solids concentration, gas velocity, and particle size in a gas–liquid–solid column system. Their results showed that the bubble size distribution shifted from bimodal to unimodal, which in turn affected separation behavior, and they identified a distinct critical coalescence concentration (CCC). Kim and Park (2024) reported key quantitative metrics in column flotation, such as $d_{32} \approx 0.62$ mm and CCC ≈ 120 ppm, and incorporated the product of gas flow rate and bubble diameter into a gas-dispersion index to predict bubble behavior and trends in Sb. From a process-performance perspective, Jameson's work demonstrated that bubble loading exerts a decisive influence on coarse-particle recovery and further proposed a "loading–

DOI: 10.37190/ppmp/215005

flotation–froth passage" constraint mechanism, thereby linking bubble-scale effects to macroscopic recovery curves (Jameson and Emer, 2024).

Accurate measurement of bubble motion characteristics is a prerequisite for further investigation. Although conventional high-speed photography and shadow imaging have been widely employed, they are constrained by two-dimensional projection, depth-of-field, and lens distortion effects, often leading to systematic errors in diameter and aspect ratio (Vinnett and Mesa, 2023), which require rigorous camera calibration and optical design for correction (Tian and Waller, 2010). To overcome the limitations of two-dimensional measurements, virtual stereoscopic vision enables three-dimensional reconstruction of bubbles, allowing simultaneous acquisition of rise velocity and orientation evolution. Digital holography, in turn, captures bubble coalescence and shear-induced breakup over a larger field of view, making it suitable for high-throughput observations. When combined with meticulous radial-distortion modeling and telecentric optical configurations, these approaches can markedly enhance the accuracy and traceability of bubble parameters (Zhang, 2000).

In iron ore flotation, column cationic reverse flotation (in which quartz is floated and hematite sinks to the tailing stream) applied to hematite-quartz systems is particularly sensitive to bubble size and froth stability. Recent studies on environmentally benign reagents and their synergistic formulations have demonstrated potential to improve bubble loading and froth stability, thereby enhancing hematite separation efficiency (Gouvêa Junior et al., 2023; Zhao et al., 2024). Building on the hematite column cationic reverse flotation process previously developed by our research group (Wang and Han, 2020), this study establishes a virtual stereoscopic vision platform to systematically investigate the three-dimensional evolution of the bubble velocity, aspect ratio, and size under realistic flotation conditions. This work quantitatively elucidates the effects of GE-609 and equipment parameters on bubble behavior, providing experimental evidence and mechanistic insights for process optimization and equipment design improvement.

2. Experimental section

2.1. Experimental platform

To mitigate measurement biases arising from temporal asynchrony and geometric distortion inherent in two-dimensional imaging, and to obtain traceable three-dimensional bubble kinematic parameters, we constructed a virtual binocular stereovision measurement platform tailored for flotation systems. Because the two cameras cannot be ensured to capture the same instantaneous bubble state, a stereovision configuration was adopted following established virtual binocular imaging practices (Augustyniak et al., 2020; Augustyniak and Perkowski, 2021). As shown in Fig. 1a, the platform comprises two major components: an image-acquisition unit and a bubble-generation unit. A two-dimensional schematic diagram is provided in Fig. 1b to more clearly illustrate the spatial layout of the experimental system. The image-acquisition unit consists of two high-speed cameras, LED backlight sources, a diffuser plate, and a computer, while the bubble-generation unit includes a precision syringe pump, a reflecting mirror, and a laboratory-scale flotation column. The high-speed cameras were operated at 500 frames per second with an image resolution of 1600×1200 pixels, and the raw bubble images were simultaneously recorded to the computer. The laboratory-scale flotation column used in this study is a transparent cylindrical column with an inner diameter of 50 mm and an effective liquid height of 600 mm, providing sufficient rising distance for bubble kinematic measurement while minimizing wall effects.

To obtain high-contrast bubble images with sharply defined edges, a backlit imaging configuration was employed. A 28 W LED light source was positioned behind the flotation column, and a uniformly transmitting diffuser plate was placed in front of the LED light source to provide stable, spatially uniform illumination and thus avoid local glare that could compromise bubble-edge detection. To minimize geometric distortion, the LED, diffuser, model flotation column, and high-speed camera were strictly aligned on the same horizontal plane, and the camera was adjusted so that its field of view was parallel to the central axis of the column. In addition, the gas flow rate was precisely regulated by an XMPS-2C precision syringe pump to ensure stable bubble generation and a consistent size distribution, thus ensuring reliable conditions for subsequent velocity and morphology analyses.

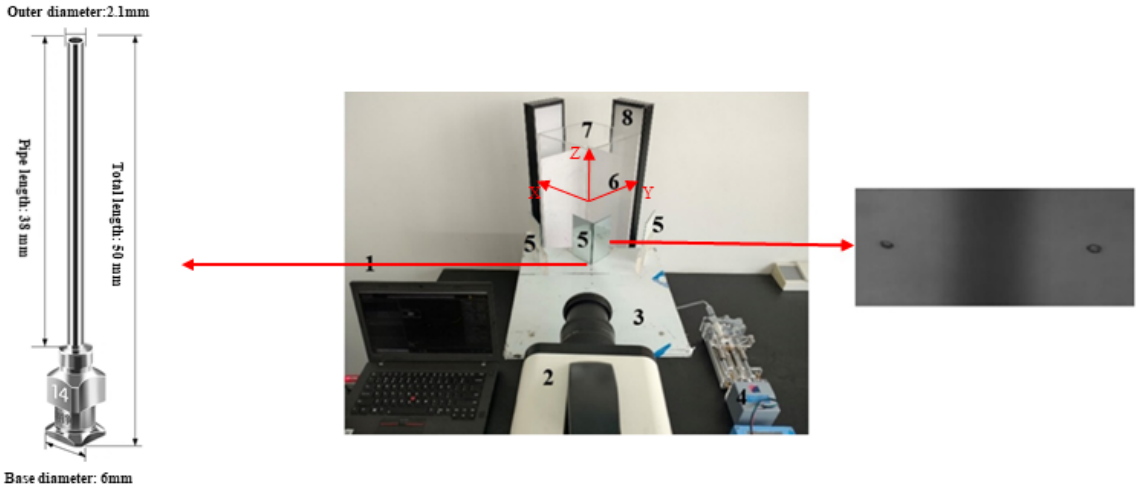

Fig. 1a. Schematic diagram of the virtual binocular stereo vision platform. 1-Computer; 2-High-speed camera; 3-Lifting table; 4-Precision syringe pump; 5-Reflector; 6- Light diffuser (Diffuser plate); 7-Analog flotation column; 8-LED light

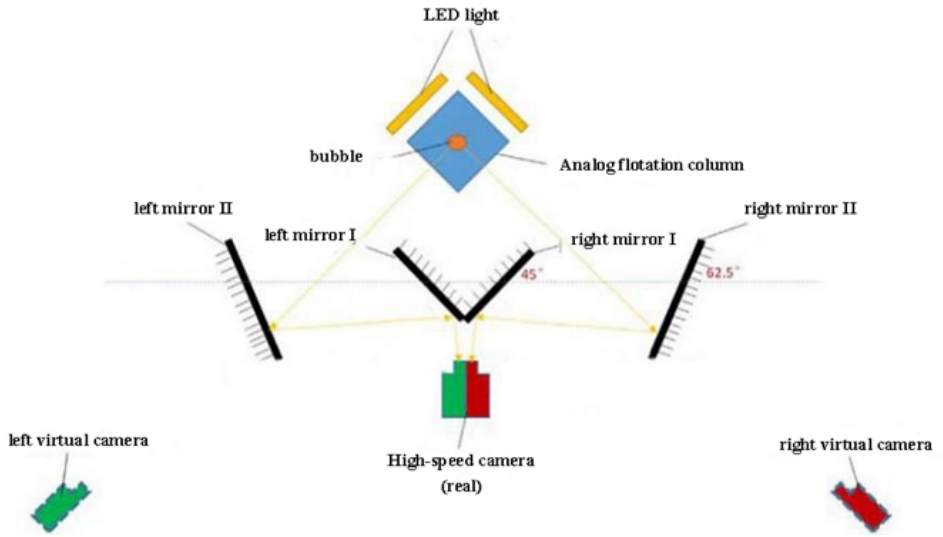

Fig. 1b. Schematic diagram of a two-dimensional structure

2.2. Experimental reagents

GE-609, a cationic collector developed at Wuhan University of Technology, is a novel ether-amine reagent; its molecular structure is shown in Fig. 2 (Zhang et al., 2025). This reagent has previously been used as a collector in the reverse cationic flotation of hematite and exhibits pronounced frothing capability; within an appropriate dosage window, it can act dually as collector and frother (Han et al., 2023b). To avoid formulation confounding introduced by adding a separate frother, no commercial frother was used in this study. Instead, GE-609 served as the sole surfactant in the system, and we specifically evaluated how its frothing action influences bubble kinematic descriptors-size, velocity, and morphology-in the flotation pulp. Variables associated with its collecting function were held constant to enable a single-factor analysis.

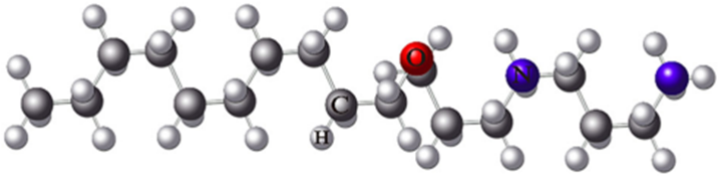

Fig. 2. Schematic diagram of the GE-609 molecular model

3. Materials and methods

3.1. Bubble image processing

Although the bubble images were obtained from two mutually orthogonal lines of sight, inferring their three-dimensional geometry from two-dimensional measurements still requires a robust parameterization procedure and reasonable geometric assumptions. In this work, the raw experimental sequences were imported into MATLAB, and a processing pipeline was established consisting of preprocessing-morphology-feature extraction. First, a background reference frame was subtracted from each image to suppress stationary textures and nonuniform illumination, followed by histogram stretching and gamma correction to enhance bubble–background contrast. Median or guided filtering was then applied to reduce salt-and-pepper and speckle noise, after which adaptive thresholding was used to produce binary masks. Bright cavities inside translucent bubbles were filled, and a combination of opening/closing operations and edge detection was employed to close contours and remove spurious spikes or fractures. Finally, at the connected-component level, geometric descriptors such as centroid, equivalent diameter, and principal axes of the outlines were extracted, providing consistent inputs for stereo matching, aspect-ratio estimation, and subsequent 3-D reconstruction. The workflow assumes that, locally, a single bubble is approximately axisymmetric, has only a small tilt, and that the two views are synchronously exposed, thereby ensuring comparability and traceability of parameters across different fields of view (Araujo et al., 2005; Maldonado et al., 2013). As an example, Fig. 3 illustrates the processing steps and key intermediate results for a representative bubble in the right-hand view.

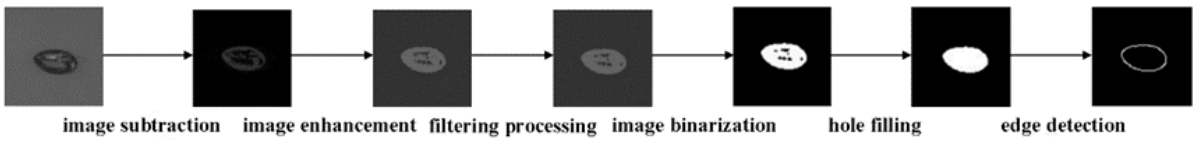

Fig. 3. Image processing flowchart

After the raw bubble images were processed through the above workflow, MATLAB was used to extract key geometric parameters, including perimeter, projected area, major and minor axes, and centroid coordinates; selected detailed results are summarized in Table 1. As shown in the table, compared with conventional photographic methods, the virtual binocular stereovision platform provides a more comprehensive set of bubble descriptors.

Table 1. Bubble parameter extraction results

Time (s)	Bubble	Perimeter (px)	Area (px²)	Long axis (px)	Short Axis (px)	Centroid(px,px)
0.000	left bubble	141.65	1392	54.26	32.95	357.280,1157.365
	right bubble	148.82	1528	58.05	33.64	1238.325,1166.356
0.002	left bubble	149.04	1592	55.41	36.68	349.909,1106.905
	right bubble	156.94	1450	55.43	33.79	1206.392,1110.759
0.004	left bubble	142.42	1357	54.66	31.82	323.036,1057.653
	right bubble	153.65	1612	56.94	36.18	1183.382,1062.997

3.2. Bubble parameters

On the basis of obtaining the perimeter, area, long axis, short axis, and center of mass parameters of the bubble, the equivalent diameter, aspect ratio, and velocity of the bubble can be calculated by Eqs. (1) to (6) (Zhang et al., 2019).

$$D = 2\sqrt{\frac{S_R+S_L}{2\pi}} \tag{1}$$

where S_L is the area of the left bubble, S_R is the area of the right bubble, and D is the equivalent diameter of the bubble.

$$E = \frac{B_L + B_R}{A_L + A_R} \tag{2}$$

where A_L is the major axis of the left bubble, A_R is the major axis of the right bubble, B_L is the minor axis of the left bubble, B_R is the minor axis of the right bubble, and E is the bubble aspect ratio.

$$V_x = \frac{\bar{x}_{i+1} - \bar{x}_i}{\Delta t} \tag{3}$$

$$V_y = \frac{\bar{y}_{i+1} - y_i}{\Delta t} \tag{4}$$

$$V_z = \frac{\bar{z}_{i+1} - z_i}{\Delta t} \tag{5}$$

$$V = \sqrt{V_x^2 + V_y^2 + V_z^2} \tag{6}$$

where $(\bar{x}_i, \bar{y}_i, \bar{z}_i)$- the bubble centroid coordinates at time t_i, $(\bar{x}_{i+1}, \bar{y}_{i+1}, \bar{z}_{i+1})$- the bubble centroid coordinates at time t_{i+1}, V_x is the velocity of the bubble in the X direction, V_y is the velocity of the bubble in the Y direction, V_z is the velocity of the bubble in the Z direction.

3.3. Coordinate system conversion

The conversion from two-dimensional to three-dimensional coordinates is achieved through a series of coordinate system transformations, as illustrated in Fig. 4. First, the world coordinate system is rigidly transformed into the camera coordinate system. The data are then projected onto the image coordinate system using a perspective model and, finally, converted into the pixel coordinate system (Salvi et al., 2002; Song et al., 2018). Based on the bubble's two-dimensional centroid parameters, its three-dimensional centroid coordinates can be determined. By subtracting the coordinates of successive centroids and dividing by the elapsed time, the bubble velocity is obtained.

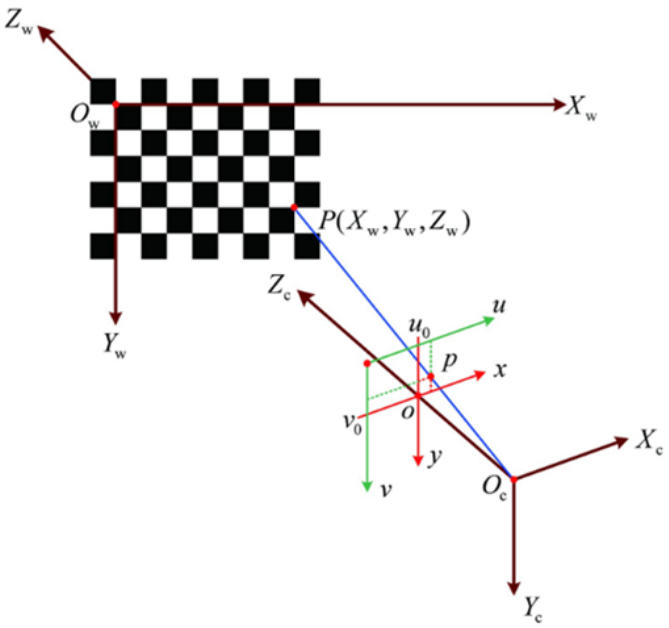

Fig. 4. Schematic diagram of spatial coordinate transformation. O_w–$X_wY_wZ_w$: world coordinate system; O_c–$X_cY_cZ_c$: camera coordinate system; P(X_w, Y_w, Z_w): a point in the world coordinate system; p: projection of P on the image plane;(x, y): image-plane coordinates; (u, v): pixel coordinates; (u_0, v_0): principal point

4. Results and discussion

4.1. Effect of different operating conditions on bubble velocity

4.1.1. Effect of agent concentration on bubble velocity

GE-609 concentration is one of the key factors influencing bubble velocity. To systematically evaluate its effect, experiments were conducted under a constant gas flow rate of 0.02 cm^3/s and a bubble generator orifice diameter of 0.6 mm. GE-609 concentration was adjusted to 1, 2, 3, 4, and 5 mg/dm^3,

and the resulting changes in bubble velocity along different directions were examined. The relationship between GE-609 concentration and bubble velocity is presented in Fig. 5.

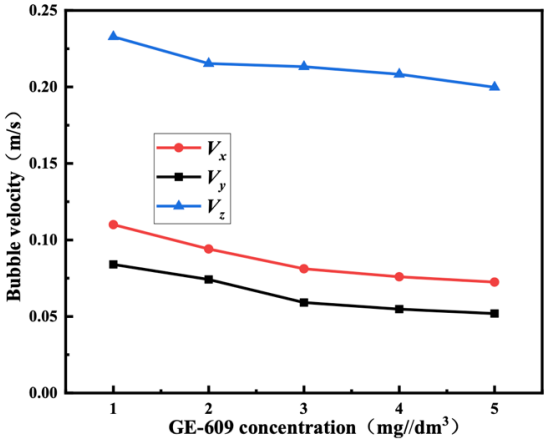

Fig. 5. Effect of GE-609 concentration on the velocity of bubbles in different coordinate axes

As shown in Fig. 5, the bubble exhibits its highest velocity along the Z-axis, followed by the X-axis and the Y-axis. The velocities in the X- and Y-directions are relatively close compared with that in the Z-direction, which is attributed to the bubble's helical trajectory during ascent. This helical motion is induced by asymmetric pressure distribution and unsteady vortex shedding around the bubble interface, causing lateral forces that continuously shift its horizontal position. As a result, the bubble does not rise strictly vertically but follows a spiral path, which leads to non-zero velocity components in the X and Y directions. When projected onto the horizontal plane, the bubble path approximates an elliptical trajectory, resulting in slightly different velocity magnitudes along the X- and Y-axes. As the GE-609 concentration increases, the bubble velocity along all three axes decreases, with the most pronounced reduction observed when the concentration increases from 1 mg/dm^3 to 2 mg/dm^3.

To gain deeper insight into the variation in bubble velocity within the flotation system, the instantaneous velocity of bubbles was also examined. The high-speed camera was set to 500 fps (frames per second), and a sequence of 100 bubble images was processed to determine the velocity profile over a 0.2 s interval. The results are presented in Fig. 6.

As shown in Fig. 6, the instantaneous velocity of a rising bubble is not constant but fluctuates about a mean value in a cyclic manner. This fluctuation results from the periodic deformation of the bubble and the unsteady vortex shedding in its wake, which generate alternating drag forces and cause oscillatory velocity dynamics. Similar periodic behavior is also observed in the aspect-ratio evolution (Fig. 9), indicating a strong coupling between bubble deformation and motion during ascent. The peaks and troughs of the curve correspond to the bubble's maximum and minimum instantaneous velocities, respectively. As the GE-609 concentration increases, the instantaneous velocity exhibits an overall decreasing trend, and both the maximum and minimum values decline accordingly. This behavior is consistent with the effect of GE-609 concentration on bubble velocity along different axes, with the most pronounced reduction occurring as the concentration increases from 1 mg/dm^3 to 2 mg/dm^3.

The periodic fluctuation of instantaneous bubble velocity observed in Fig. 6 agrees with the findings of Magnaudet and Eames (2000) and Clift et al. (1978), who reported similar oscillatory rising behavior of bubbles due to unsteady vortex shedding and deformation during ascent. The periodic peaks and troughs in Fig. 6 reflect alternating drag forces caused by vortex shedding, supporting the physical mechanism reported in these earlier studies and confirming the reliability of the stereovision velocity measurement method.

4.1.2. Effect of bubble generator aperture on bubble velocity

In a previous study, a scanning electron microscope (SEM) was used to characterize the pore-size distribution of a bubble generator employed in a microbubble counter-current contact flotation column, where the pore diameters ranged from 51.715 μm to 502.780 μm (Wang and Han, 2020). Guided by this pore-size range, the present work selected bubble-generator apertures of 200, 400, and 600 μm (i.e., 0.2,

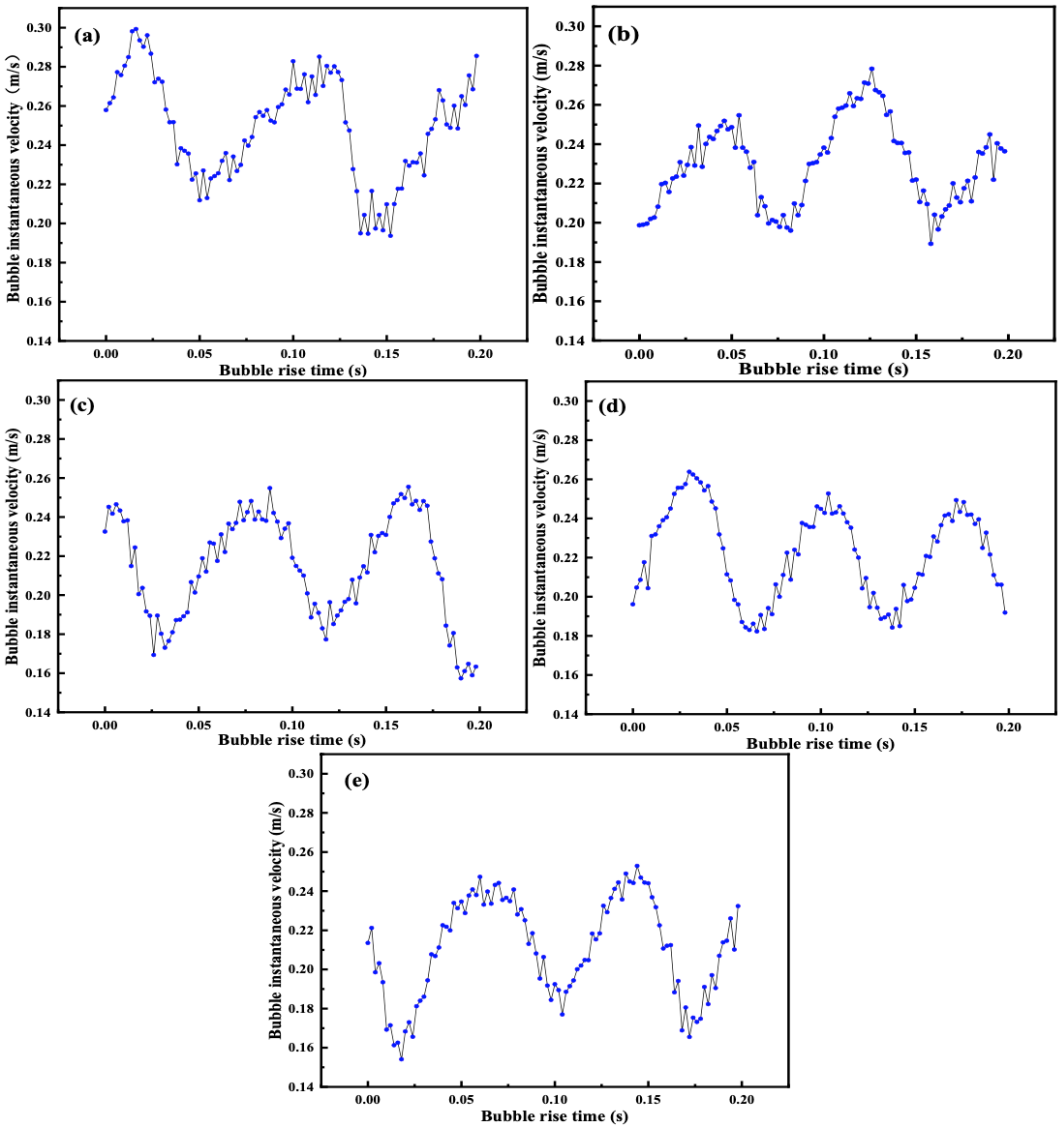

Fig. 6. Effect of GE-609 concentration on the instantaneous velocity of bubbles (a) GE-609 concentration 1 mg/dm³; (b) GE-609 concentration 2 mg/dm³; (c) GE-609 concentration 3mg/dm³;(d) GE-609 concentration 4mg/dm³; (e) GE-609 concentration 5 mg/dm³

0.4, and 0.6 mm) as representative small, medium, and large scales to investigate their influence on bubble kinematics under controlled single-bubble release conditions and enable clear comparative analysis across different aperture sizes. The bubble generator used in this work is a commercially manufactured micro-orifice gas distributor designed to produce discrete bubbles under controlled single-bubble release conditions, as illustrated in Fig. 1. Bubble velocities along the *X*-, *Y*-, and *Z*-directions measured using the stereovision platform are compared in Fig. 7, where d_0 denotes the aperture of the micro-orifice distributor. To ensure accurate quantitative tracking and to avoid bubble–bubble interactions, all measurements were conducted under single-bubble release operating conditions.

In contrast to Fig. 5, which presents the three directional velocity components under varying GE-609 concentrations, Fig. 7 additionally includes the resultant bubble velocity (V), defined as eq. (6), to illustrate the comprehensive effect of aperture size on bubble motion.

The decreasing trend in bubble velocity with reduced aperture size shown in Fig. 7 is consistent with the observations of Yoon (1989) and Jameson (2013), who demonstrated that smaller bubble-generator orifices produce smaller bubbles with higher drag resistance and therefore lower rising velocity. This correspondence indicates that the aperture-dependent variation captured in Fig. 7 reflects realistic bubble kinematic behavior in flotation systems.

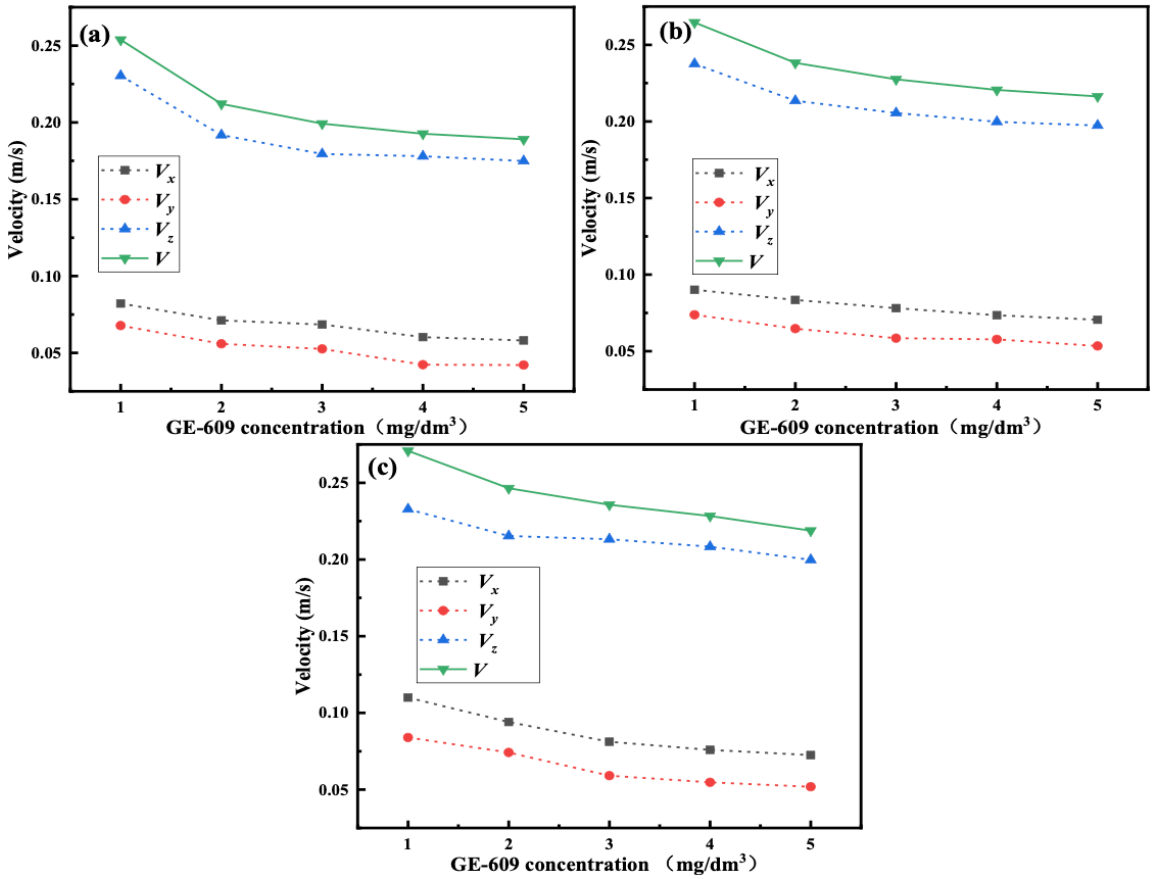

Fig. 7. Bubble velocity diagram. (a) d_0=0.2 mm; (b) d_0=0.4 mm; (c) d_0=0.6 mm. V_x, V_y, and V_z represent the velocity components along the *X*-, *Y*-, and *Z*-directions, and V denotes the resultant velocity

4.2. Relationship between bubble velocity and other bubble parameters

4.2.1. Relationship between bubble velocity and bubble size

In this work, bubble size was characterized by the equivalent diameter. At a fixed aeration rate of 0.02 cm³/s and the GE-609 concentration of 2 mg/dm³, the relationship between bubble velocity and equivalent diameter was examined under bubble-generator apertures of 0.2, 0.4, and 0.6 mm (Fig. 8). The results show that bubble velocity increases with equivalent diameter, and this monotonic trend is consistent across all three apertures, indicating that rising velocity is mainly governed by the bubble's actual size and interfacial condition rather than by the initial nucleation aperture.

From a mechanical perspective, bubble velocity during the quasi-steady rising stage is determined by the balance between buoyancy and drag. Larger bubbles experience greater buoyancy and larger wake dimensions; although drag also increases with size, the combined effects of interfacial properties and wake structure allow the slip velocity to rise overall. Dimensionless analysis reveals that both Reynolds and Eötvös numbers grow with size, while the bubble shape evolves from nearly spherical to oblate ellipsoidal. The resulting changes in drag coefficient account for the observed positive velocity–size correlation.

GE-609 concentration shifts the velocity-size curve downward and reduces its slope. Adsorption of GE-609 molecules at the gas–liquid interface induces a Marangoni effect, enhances interfacial shear, and suppresses bubble coalescence, thereby lowering velocity at a given diameter. When the concentration increases from 1 to 2 mg/dm³, the decrease in velocity is most pronounced, after which the slope flattens, reflecting diminishing marginal effects once interfacial "contamination" or rigidification approaches saturation.

The similarity in curve shape under different apertures indicates a certain scale invariance of the velocity–size function: aperture mainly affects the initial bubble-size distribution and release frequency, while the intrinsic relationship between velocity and equivalent diameter remains unchanged. Overall,

at fixed aeration and baseline concentration, bubble velocity shows a robust positive correlation with equivalent diameter, whereas higher GE-609 concentration shifts the curve downward and weakens its marginal effect. These findings provide a theoretical basis for controlling interfacial cleanliness and target size distribution to regulate bubble rising velocity and, consequently, particle–bubble collision probability.

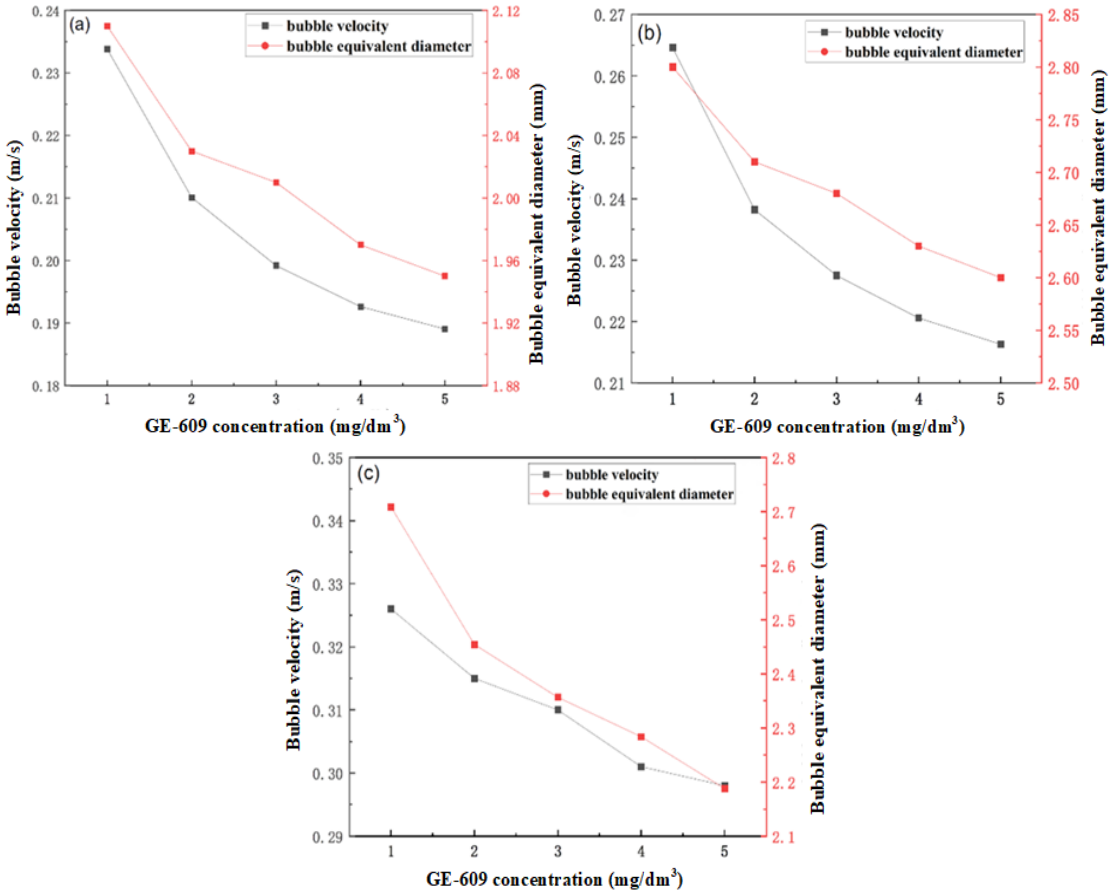

Fig. 8. Relationship between bubble velocity and equivalent diameter of the bubble. (a) d_0=0.2mm; (b) d_0=0.4mm; (c) d_0=0.6mm

The positive correlation between bubble velocity and equivalent diameter shown in Fig. 8 is consistent with the findings of Maldonado et al. (2013), who experimentally reported that larger bubbles experience greater buoyancy and wake development, leading to higher slip velocities during ascent. Similar monotonic trends have also been described by Panjipour et al. (2021), who demonstrated that increasing bubble size shifts the velocity distribution upward in bubble columns. These consistencies confirm that the measured velocity–size scaling reflects authentic hydrodynamic behavior and further validate the applicability of the stereovision approach to quantify bubble motion under flotation-relevant conditions.

4.2.2. Relationship between bubble velocity and bubble aspect ratio

Taking a bubble-generator aperture of 0.6 mm as an example, the relationship between instantaneous bubble velocity and aspect ratio during ascent was analyzed under different GE-609 concentrations. The results are presented in Fig. 9, where panels (a)–(e) correspond to GE-609 concentrations of 1, 2, 3, 4, and 5 mg/dm^3, respectively. At all concentrations, the instantaneous velocity shows a clear negative correlation with the aspect ratio: velocity peaks generally coincide with troughs of the aspect ratio, indicating a strong coupling between bubble deformation and motion during rise. The velocity fluctuates about its mean value, while the aspect ratio varies periodically in phase, suggesting that even in the quasi-steady rising stage, the bubble's hydrodynamic forces and interfacial shape remain in a dynamic balance rather than a static state.

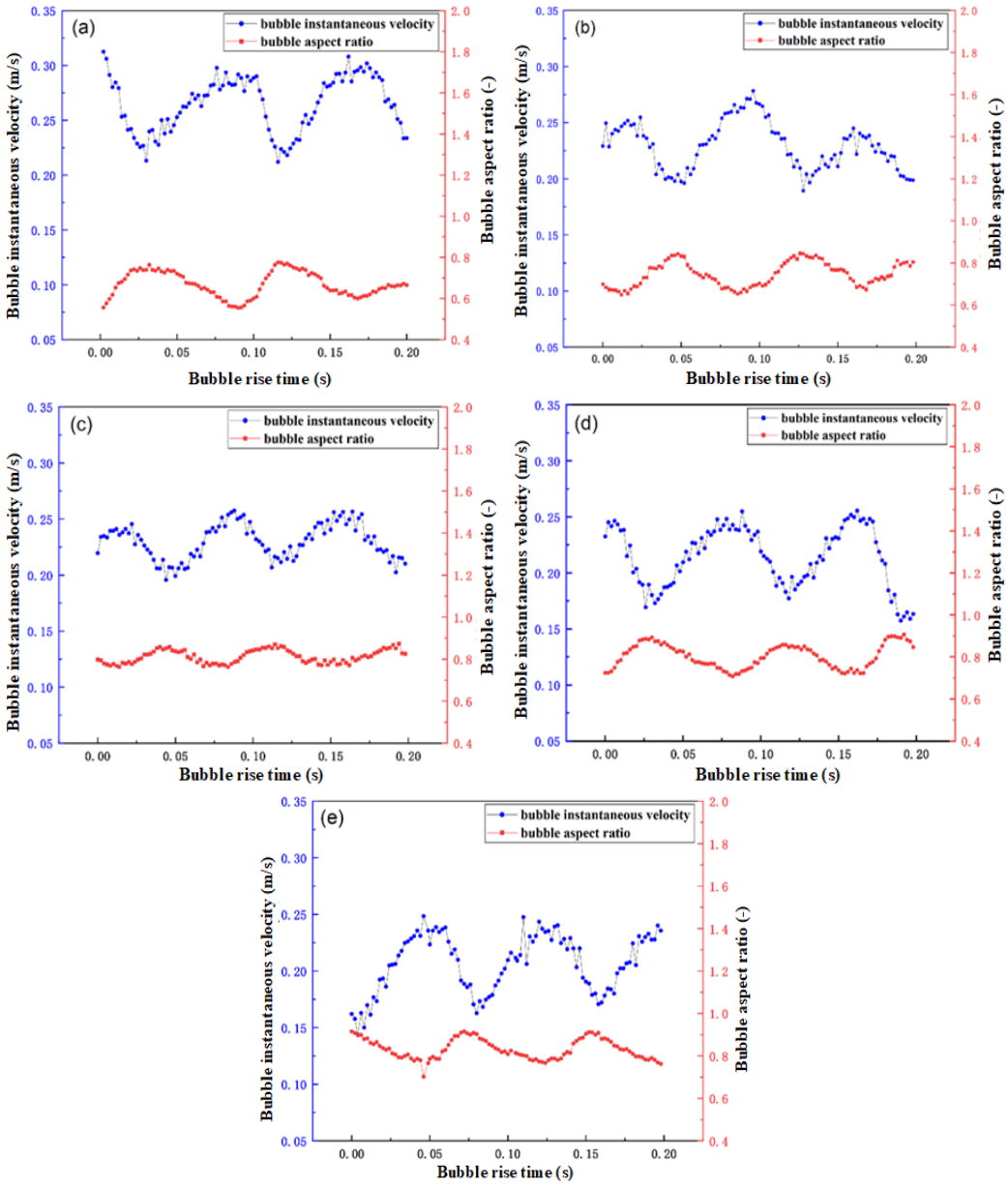

Fig. 9. Relationship between bubble velocity and aspect ratio. (a) GE-609 concentration 1 mg/dm³; (b) GE-609 concentration 2 mg/dm³; (c) GE-609 concentration 3 mg/dm³; (d) GE-609 concentration 4mg/dm³; (e) GE-609 concentration 5 mg/dm³

As the GE-609 concentration increases, the overall rising velocity decreases, and the amplitudes of both velocity and aspect-ratio oscillations are reduced. This indicates that adsorption of GE-609 molecules at the gas–liquid interface suppresses interfacial tension gradients and weakens bubble deformation and oscillation. When the concentration increases from 1 to 2 mg/dm³, the reduction in velocity is most pronounced; with further increases, the changes in velocity and aspect ratio become more gradual, implying that once interfacial adsorption approaches saturation, its additional impact on bubble dynamics is limited. Overall, after entering a stable rising regime, the bubble's velocity and aspect ratio fluctuate regularly around their respective mean values, a behavior closely related to vortex formation on the bubble surface and asymmetry in the wake during ascent. Moderate periodic oscillation helps maintain relative motion between the bubble and surrounding fluid, whereas excessive GE-609 concentration tends to "rigidify" the interface, dampen oscillations, and further reduce the rising velocity.

The strong negative correlation between instantaneous bubble velocity and aspect ratio observed in Fig. 9 aligns with the results of Liu et al. (2021), who reported that bubble elongation is closely linked

to wake asymmetry and transient variations in drag. Likewise, Augustyniak et al. (2020) demonstrated that oscillatory deformation induces multifractal bubble-path dynamics, reinforcing the interpretation that bubble motion is inherently unsteady even during quasi-steady rising stages. These comparisons support the conclusion that deformation-induced hydrodynamic coupling is a fundamental mechanism governing bubble-motion stability in flotation systems.

5. Conclusions

Based on experiments conducted using a virtual binocular stereovision platform, this study quantitatively examined the velocity, size, and deformation characteristics of flotation bubbles, as well as the effects of GE-609 concentration and bubble-generator aperture on bubble kinematics. The main conclusions are as follows:

(1) Bubble rise velocity decreases progressively with increasing GE-609 concentration, with the most pronounced reduction occurring as the concentration increases from 1 to 2 mg/dm^3, reflecting enhanced interfacial adsorption effects at lower concentrations. The vertical (Z-axis) component consistently dominates the overall rise velocity, and the instantaneous velocity exhibits clear periodic fluctuations caused by helical rising motion and alternating hydrodynamic forces.

(2) Bubble velocity increases significantly with larger bubble-generator apertures because larger bubbles experience stronger buoyancy and reduced drag, leading to higher rise velocities. This finding indicates that tailoring the structural parameters of the bubble generator can effectively regulate bubble kinematics and improve bubble transport within flotation columns.

(3) Peaks in instantaneous velocity coincide with minima in aspect ratio, demonstrating a stable negative correlation between velocity and deformation. Bubble velocity is positively correlated with equivalent diameter, independent of aperture size or GE-609 concentration, indicating that bubble size is the dominant parameter governing bubble motion behavior. These results clarify the mechanisms by which operational and equipment parameters influence bubble dynamics and provide experimental guidance for optimizing flotation operating conditions, controlling collector dosage, and designing efficient bubble-generation systems.

In future work, the stereovision platform will be further applied to complex bubble–particle interaction systems to investigate collision, attachment, and detachment behaviors under realistic flotation conditions. Besides, integrating multiphase hydrodynamic modeling with experimental measurements may provide deeper insight into bubble dynamics and support flotation equipment design optimization.

Acknowledgments

This research was funded by the Yanzhao Iron and Steel Laboratory Regional Innovation Ability Promotion Project (YZISL2024051).

References

ARAUJO, A.C., VIANA, P.R.M., PERES, A.E.C., 2005. *Reagents in iron ores flotation*. Minerals Engineering, 18(2), 219-224.

AUGUSTYNIAK, J., PERKOWSKI, D.M., 2021. *Compound analysis of gas bubble trajectories with the help of a multifractal algorithm*. Experimental Thermal and Fluid Science, 124, 121-136.

AUGUSTYNIAK, J., PERKOWSKI, D.M., MOSDORF, R., 2020. *Measurement of multifractal character of bubble paths using image analysis*. International Communications in Heat and Mass Transfer, 117, 37-52.

CLIFT, R., GRACE, J.R., WEBER, M.E., 1978. *Bubbles, Drops, and Particles.* Academic Press, New York.

HAN, J., LI, Y., CHEN, P., 2023. *A study of bubble size/shape evolution in microbubble countercurrent contacting flotation column*. Asia-Pacific Journal of Chemical Engineering, 18(2), e2865.

HAN, J., CHEN, P., LIU, T., LI, Y., 2023. *Research and application of fluidized flotation units: A review*. Journal of Industrial and Engineering Chemistry, 126, 50-68.

GOUVÊA JUNIOR, J.T., CHIPAKWE, V., LEAL FILHO, L.S., CHEHREH CHELGANI, S., 2023. *Biodegradable ether amines for reverse cationic flotation separation of ultrafine quartz from magnetite*. Scientific Reports, 13, 21010.

JAMESON, G.J., 2013. *Advances in fine and coarse particle flotation*. Canadian Metallurgical Quarterly, 49(5), 325-330.

JAMESON, G.J., EMER, C., 2024. *Effect of bubble loading on the recovery of coarse mineral particles by flotation.* Minerals Engineering, 215, 108788.

KIM, H.S., PARK, C.-H., 2024. *Estimation of bubble size and gas dispersion property in column flotation*. Chemosensors, 11, 331.

LIU, L., ZHANG, H., YAN, H., ZIEGENHEIN, T., HESSENKEMPER, H., ZHOU, P., LUCAS, D., 2021. *Experimental studies on bubble aspect ratio and corresponding correlations under bubble swarm condition.* Chemical Engineering Science, 236, 116551.

MAGNAUDET, J., EAMES, I., 2000. *The motion of high-Reynolds-number bubbles in inhomogeneous flows*. Annual Review of Fluid Mechanics, 32, 659-708.

MALDONADO, M., ERVINE, D., RALSTON, J., 2013. *An experimental study examining the relationship between bubble shape and rise velocity*. Chemical Engineering Science, 98, 7-11.

PANJIPOUR, R., KARAMOOZIAN, M., ALBIJNIC, B., 2021. *Bubble size distributions in gas–liquid–solid systems and their influence on flotation separation in a bubble column.* Chemical Engineering Research and Design, 169, 148-162.

SALVI, J., ARMANGUÉ, X., BATLLE, J., 2002. *A comparative review of camera calibrating methods with accuracy evaluation*. Pattern Recognition, 35(7), 1617-1635.

SONG, K.C., HOU, B., NIU, M.H., et al., 2018. *Flexible line-scan camera calibration method using a coded eight trigrams pattern*. Optics and Lasers in Engineering, 110, 296-307.

TIAN, L., WALLER, L., 2010. *Quantitative measurement of size and 3D position of fast-moving bubbles using digital holography*. Applied Optics, 49, 1549-1554.

VINNETT, L., MESA, D., 2023. *A discussion on the limitations of image analysis for determining bubble size in industrial flotation*. Physicochemical Problems of Mineral Processing, 59, 174474.

WANG, W., HAN, J., 2020. *Study on bubble characteristics of flotation column in hematite reverse cationic flotation process*. Physicochemical Problems of Mineral Processing., 56, 1: 64-75.

YOON, R.-H., LUTTRELL, G.H., 1989. *The effect of bubble size on fine particle flotation*. Mineral Processing & Extractive Metallurgy Review, 5, 101-122.

ZHANG, L., WANG, W., LIU, D., LI, D., 2025. *Study on the three-dimensional motion trajectory of bubbles in column flotation system.* Asia-Pacific Journal of Chemical Engineering, 20(6), e70052.

ZHANG, T., QIAN, Y., YIN, J., ZHANG, B., WANG, D., 2019. *Experimental study on 3D bubble shape evolution in swirl flow*. Experimental Thermal and Fluid Science, 102, 368-375.

ZHANG, Z., 2000. *A flexible new technique for camera calibration*. IEEE Transactions on Pattern Analysis and Machine Intelligence, 22, 1330-1334.

ZHAO, P., LIU, W., LIU, W., GUO, Y., 2024. *Separation of hematite and quartz in a cationic collector flotation system using Pullulan as a greener depressant.* Journal of Molecular Liquids, 410, 125643.